Multi-component Gaussian beam prestack depth migration

2013 J. Geophys. Eng. 10 055008

(http://iopscience.iop.org/1742-2140/10/5/055008)

J. Geophys. Eng. **10** (2013) 055008 (10pp) doi:10.1088/1742-2132/10/5/055008

Multi-component Gaussian beam prestack depth migration

Jianguang Han[1,2], **Yun Wang**[3,5] **and Jun Lu**[4]

[1] Institute of Geology and Geophysics, Chinese Academy of Sciences, Beijing 100029, People's Republic of China
[2] University of Chinese Academy of Sciences, Beijing 100049, People's Republic of China
[3] Institute of Geochemistry, Chinese Academy of Sciences, Guiyang 550002, People's Republic of China
[4] China University of Geosciences (Beijing), Beijing 100083, People's Republic of China

E-mail: yunwang@mail.iggcas.ac.cn

Received 22 March 2013
Accepted for publication 3 September 2013
Published 20 September 2013
Online at stacks.iop.org/JGE/10/055008

Abstract
As the depth migration of multi-component seismic data can obtain better images of the subsurface structures with multi-wave information in seismic records, an effective multi-component Gaussian beam migration method is presented in this paper. Firstly, a detailed numerical analysis on the local slant stack is carried out, which demonstrates that the Gaussian beam migration method has good directionality and computational efficiency through decomposing seismic records into different outgoing directional local plane waves. Then two different Gaussian beam prestack depth migration algorithms are presented, corresponding to the PP- and PS-waves, after a wavefield separation is effected with an affine coordinate system transform. Finally, tests of synthetic and field seismic data show that the method introduced above would be an accurate and efficient prestack depth migration alternative for multi-component seismic data.

Keywords: multi-component, Gaussian beam prestack depth migration, numerical analysis, local slant stack, wavefield separation

1. Introduction

For multi-component seismic exploration both PP- and PS-wave data can be obtained. Because these waves carry different information about target regions (Xie and Wu 2005), they may provide more petrophysical parameters and effectively improve the accuracy of seismic exploration, compared with P-wave data alone. Therefore, more effective multi-component migration techniques are required to make full use of multi-component information. There are two basic families of prestack depth migrations of multi-component seismic data: elastic migration and scalar migration (Hou and Marfurt 2002). Kirchhoff elastic wave migration was implemented by Kuo and Dai (1984) and by Dai and Kuo (1986). Hokstad (2000) extended the practice to anisotropic elastic and viscoelastic imaging of multi-component seismic data. Chang and McMechan (1987, 1994) conducted 2D and 3D elastic reverse time migrations using the finite-difference method. Meanwhile, some authors proposed scalar migration methods for multi-component seismic data by first separating the wavefield into PP- and PS-waves (Wang and Nemeth 1997, Sun and McMechan 2001, Hou and Marfurt 2002). For these migration methods, the ray-based Kirchhoff method is more efficient and flexible, but it has multi-valued travel times, which affect the migration result. The reverse time migration based on the full wave finite-difference method is more accurate. However, the method is very time consuming. Gaussian beam migration, as a powerful imaging technique, is an elegant and efficient depth migration method, with an accuracy comparable to wave-equation migration and a flexibility comparable to Kirchhoff migration (Gray and Bleistein 2009).

In the field of seismology, the Gaussian beam method for the computation of the wavefield (Červeny *et al* 1982,

[5] Author to whom any correspondence should be addressed.

2007, Popov 1982,) was first used in seismic wavefield forward modeling (Červeny 1985, Nowack 2003), and then the Gaussian beam migration method was studied. Hill (1990) proposed a Gaussian beam poststack migration method and performed a detailed study of migration parameters. Hale (1992a, 1992b) further introduced an algorithm and implementation of Gaussian beam migration. Hill (2001) presented a prestack Gaussian beam migration method that operates on common-offset and common-azimuth data volumes. Gray (2005) removed the narrow azimuth restriction by presenting variations suitable for common-shot records migration. In further publications, true-amplitude Gaussian beam migration methods were developed by Gray and Bleistein (2009) and Popov *et al* (2008, 2010). However, their studies start with a definition of the acoustic wave migration formula, without reference to elastic waves. It is not clear how the Gaussian beam migration method should be applied for multi-component seismic data recorded in elastic media.

Based on previous studies, a multi-component Gaussian beam prestack depth migration method is presented. The purpose of this paper is to provide a new effective method for multi-component seismic data migration imaging. We first introduce the distribution characteristics of wavefield energy around the Gaussian beam, and describe the Green function constructed by Gaussian beams. Next, a detailed numerical analysis on the local slant stack of the Gaussian beam migration is carried out. Then, the Gaussian beam migration imaging conditions for pure PP- and PS-waves obtained from wavefield separation in the affine coordinate system are applied. Finally, to verify the feasibility of the new multi-component Gaussian beam migration method, synthetic examples and field seismic data are tested.

2. Fundamental method

2.1. Gaussian beam theory

In the two-dimensional isotropic medium, the Gaussian beam connected with a central ray Ω can be written in ray-centered coordinate system (s, n) as (Červeny *et al* 1982, Popov 1982)

$$\mathrm{u}(s, n, \omega) = \left[\frac{V(s)}{q(s)}\right]^{\frac{1}{2}} \exp\left[\mathrm{i}\omega\tau(s) + \frac{\mathrm{i}\omega}{2}\frac{p(s)}{q(s)}n^2\right], \qquad (1)$$

where $\mathrm{u}(s, n, \omega)$ is the seismic wavefield, the coordinate s measures the arc length along the ray Ω from an arbitrary reference point, and n represents the length coordinates perpendicular to the ray at s. ω is the frequency and $V(s)$ is the velocity along the central ray Ω. Function $\tau(s)$ is the travel time along the central ray. $p(s)$ and $q(s)$ are complex solutions to dynamic ray tracing equations (Červeny 2007), which determine the energy distribution of Gaussian beam and contain the dynamic characteristics of high-frequency seismic wave propagation along the ray. Gaussian beam expressions have the same form for P- and S-waves, and the only difference is the corresponding P- and S-wave velocities required in the calculation (Červeny 1983).

Compared with traditional ray theory, the Gaussian beam method not only involves the wavefield energy along the central ray, but also utilizes wavefields near the ray. Figure 1 shows the wavefield near a central ray simulated by Gaussian beam method. As the wave propagates along the ray direction, the wavefield energy distributes in the vicinity of the ray and gradually decays with increasing vertical distance from the central ray.

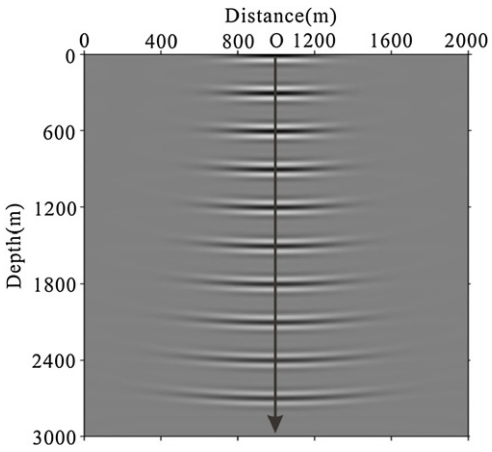

Figure 1. Gaussian beam wavefield energy distribution near a central ray emitted from a point source O in a homogeneous and isotropic medium.

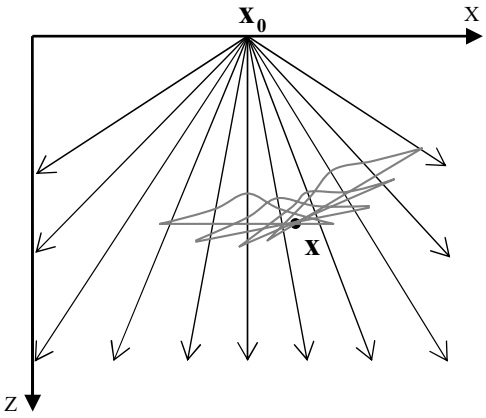

Figure 2. Sketch of Green's function in terms of Gaussian beams. The wavefield near each central ray can be calculated by Gaussian beam method and the wavefield at a point $\mathbf{x} = (x, z)$ in the subsurface is a weighted sum over the nearby beams.

2.2. Green's function as an integral over Gaussian beams

In the Gaussian beam migration approach, the 2D Green's function $G_{2\mathrm{D}}(\mathbf{x}, \mathbf{x}_0, \omega)$ is an integral over a fan of Gaussian beams with different initial dip angles emitted from the source $\mathbf{x}_0 = (x_0, 0)$, as shown in figure 2.

The Green's function in terms of Gaussian beams can be expressed as (Hill 2001, Gray and Bleistein 2009)

$$G_{2\mathrm{D}}(\mathbf{x}, \mathbf{x}_0, \omega) = \frac{\mathrm{i}}{2\pi}\int \mathrm{u}_{\mathrm{GB}}(\mathbf{x}, \mathbf{x}_0, \mathbf{p}, \omega)\frac{\mathrm{d}p_x}{p_z}, \qquad (2)$$

where $\mathbf{p} = (p_x, p_z)$ is the ray parameter vector with p_x and p_z representing the horizontal and vertical component. $\mathbf{x}_0$ is the source location and $\mathbf{x}$ is a subsurface point. As P- and S-waves have the same Gaussian beam expression form, the Green's

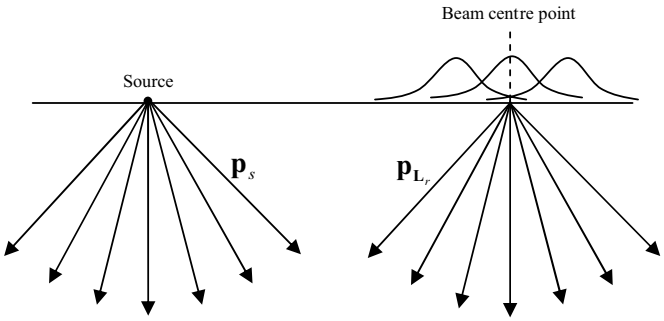

Figure 3. Sketch of Gaussian beam prestack depth migration.

function in terms of Gaussian beams can be used to describe both P- and S-wave components (Nowack *et al* 2006, 2007).

Equation (2) is an integral of individual Gaussian beams u_{GB} over horizontal slownesses p_x, and

$$u_{GB}(\mathbf{x}, \mathbf{x}_0, \mathbf{p}, \omega) = A \exp(i\omega T). \tag{3}$$

The functions A and T represent complex amplitude and complex travel time

$$A = \sqrt{\frac{V(s)q(s_0)}{V(s_0)q(s)}} \tag{4}$$

$$T = \tau(s) + \frac{n^2}{2}\frac{p(s)}{q(s)}. \tag{5}$$

The Green's function constructed from Gaussian beams is the summation of the local wavefield of limited area near the central rays, and it can solve the multi-valued travel times with different beam superpositions. Using Hill's (1990) initial data to solve the dynamic ray tracing equations can guarantee that the Gaussian beam is canonical, so the Green's function shows regular behavior at the caustics.

2.3. Multi-wave Gaussian beam prestack migration

In the multi-component seismic exploration, the *Z*- and *X*-component records can receive part of the PS- and PP-wave data, instead of the pure PP- and PS-waves. Directly using the *Z*- and *X*-components to migrate will cause wavefield crosstalk in the migration profiles. Therefore, we first separate PP- and PS-waves from multi-component seismic data with a wave vector rotation transformation method in the affine coordinate system (Lu *et al* 2012), which can recover the true amplitude of PP- and PS-waves and obtain real pure PP- and PS-waves compared with traditional wave separation methods in the Cartesian coordinate. And then the multi-component Gaussian beam prestack depth migration imaging conditions for PP- and PS-waves are presented.

A prestack migration image of Gaussian beam is formed by cross-correlating the downward-continued wavefields from source and beam centers. As shown in figure 3, the central rays of the Gaussian beam are emitted from the source and a beam center point with different ray parameters $\mathbf{p}_s$ and $\mathbf{p}_{\mathbf{L}_r}$ to compute the wavefield. For the PP-wave image, the wavefields from source and beam center points are extrapolated with P-wave velocity. For the PS-wave image downward-continued source wavefields are computed with the P-wave velocity and the S-wave velocity is used to compute the wavefields from beam center points.

In the two-dimensional isotropic medium, assume that $\mathbf{x}_s = (x_s, 0)$ and $\mathbf{x}_r = (x_r, 0)$ denote the source and receiver locations. According to the Gaussian beam prestack migration method that operates on common-offset gathers given by Hill (2001), the PP- and PS-waves common shot gathers Gaussian beam migration formula can be written as

$$I^{PP}(\mathbf{x}) = C^{PP}\int dx_s \sum_{L_r}\int d\omega \int dp_{sx}^P \int dp_{rx}^P D^{PP}\left(\mathbf{L}_r, \mathbf{p}_r^P, \omega\right) \times u_{GB}^{P*}\left(\mathbf{x}, \mathbf{x}_s, \mathbf{p}_s^P, \omega\right) u_{GB}^{P*}\left(\mathbf{x}, \mathbf{L}_r, \mathbf{p}_r^P, \omega\right) \tag{6}$$

$$I^{PS}(\mathbf{x}) = C^{PS}\int dx_s \sum_{L_r}\int d\omega \int dp_{sx}^P \int dp_{rx}^S D^{PS}\left(\mathbf{L}_r, \mathbf{p}_r^S, \omega\right) \times u_{GB}^{P*}\left(\mathbf{x}, \mathbf{x}_s, \mathbf{p}_s^P, \omega\right) u_{GB}^{S*}\left(\mathbf{x}, \mathbf{L}_r, \mathbf{p}_r^S, \omega\right), \tag{7}$$

where $I^{PP}(\mathbf{x})$ and $I^{PS}(\mathbf{x})$ are PP- and PS-wave final images at subsurface point $\mathbf{x}$. $u_{GB}^{P*}\left(\mathbf{x}, \mathbf{x}_s, \mathbf{p}_s^P, \omega\right)$ is the P-wave Gaussian beam from the source, while $u_{GB}^{P*}\left(\mathbf{x}, \mathbf{L}_r, \mathbf{p}_r^P, \omega\right)$ and $u_{GB}^{S*}\left(\mathbf{x}, \mathbf{L}_r, \mathbf{p}_r^S, \omega\right)$ are the P- and S-wave Gaussian beam wavefield formulae from the beam center point $\mathbf{L}_r = (L_r, 0)$. C^{PP} and C^{PS} denote corresponding constants. $D^{PP}\left(\mathbf{L}_r, \mathbf{p}_r^P, \omega\right)$ and $D^{PS}\left(\mathbf{L}_r, \mathbf{p}_r^S, \omega\right)$ are the local plane wave components of PP- and PS-waves, which are obtained from a local slant stack of the common-shot traces, and the expression can be written as

$$D^{PP}\left(\mathbf{L}_r, \mathbf{p}_r^P, \omega\right) = \frac{1}{4\pi^2}\left|\frac{\omega}{\omega_r}\right|^3 \int dx_r u^{PP}(\mathbf{x}_r, \mathbf{x}_s, \omega) \times \exp\left[-i\omega p_{rx}^P(x_r - L_r) - \frac{1}{2}\left|\frac{\omega}{\omega_r}\right|\frac{|x_r - L_r|^2}{L_0^2}\right] \tag{8}$$

$$D^{PS}\left(\mathbf{L}_r, \mathbf{p}_r^S, \omega\right) = \frac{1}{4\pi^2}\left|\frac{\omega}{\omega_r}\right|^3 \int dx_r u^{PS}(\mathbf{x}_r, \mathbf{x}_s, \omega) \times \exp\left[-i\omega p_{rx}^S(x_r - L_r) - \frac{1}{2}\left|\frac{\omega}{\omega_r}\right|\frac{|x_r - L_r|^2}{L_0^2}\right], \tag{9}$$

where L_0 is the initial beam width at a reference frequency ω_r (Hill 1990, Hale 1992a). $u^{PP}(\mathbf{x}_r, \mathbf{x}_s, \omega)$ and $u^{PS}(\mathbf{x}_r, \mathbf{x}_s, \omega)$ are the recorded wavefields of PP- and PS-waves.

If P- and S-wave Gaussian beam expressions are inserted into equations (6) and (7), respectively, equations (6) and (7) can be rewritten as

$$I^{PP}(\mathbf{x}) = C^{PP}\int dx_s \sum_{L_r}\int d\omega D^{PP}\left(\mathbf{L}_r, \mathbf{p}_r^P, \omega\right) \times \int dp_{sx}^P \int dp_{rx}^P \overline{A}^{PP}\left(\mathbf{x}, \mathbf{p}_s^P, \mathbf{p}_r^P\right) \exp\left[-i\omega \overline{T}^{PP}\left(\mathbf{x}, \mathbf{p}_s^P, \mathbf{p}_r^P\right)\right], \tag{10}$$

$$I^{PS}(\mathbf{x}) = C^{PS}\int dx_s \sum_{L_r}\int d\omega D^{PS}\left(\mathbf{L}_r, \mathbf{p}_r^S, \omega\right) \times \int dp_{sx}^P \int dp_{rx}^S \overline{A}^{PS}\left(\mathbf{x}, \mathbf{p}_s^P, \mathbf{p}_r^S\right) \exp\left[-i\omega \overline{T}^{PS}\left(\mathbf{x}, \mathbf{p}_s^P, \mathbf{p}_r^S\right)\right], \tag{11}$$

where functions $\overline{A}^{PP}\left(\mathbf{x}, \mathbf{p}_s^P, \mathbf{p}_r^P\right)$ and $\overline{T}^{PP}\left(\mathbf{x}, \mathbf{p}_s^P, \mathbf{p}_r^P\right)$ are the PP-wave complex amplitude and complex travel time determined

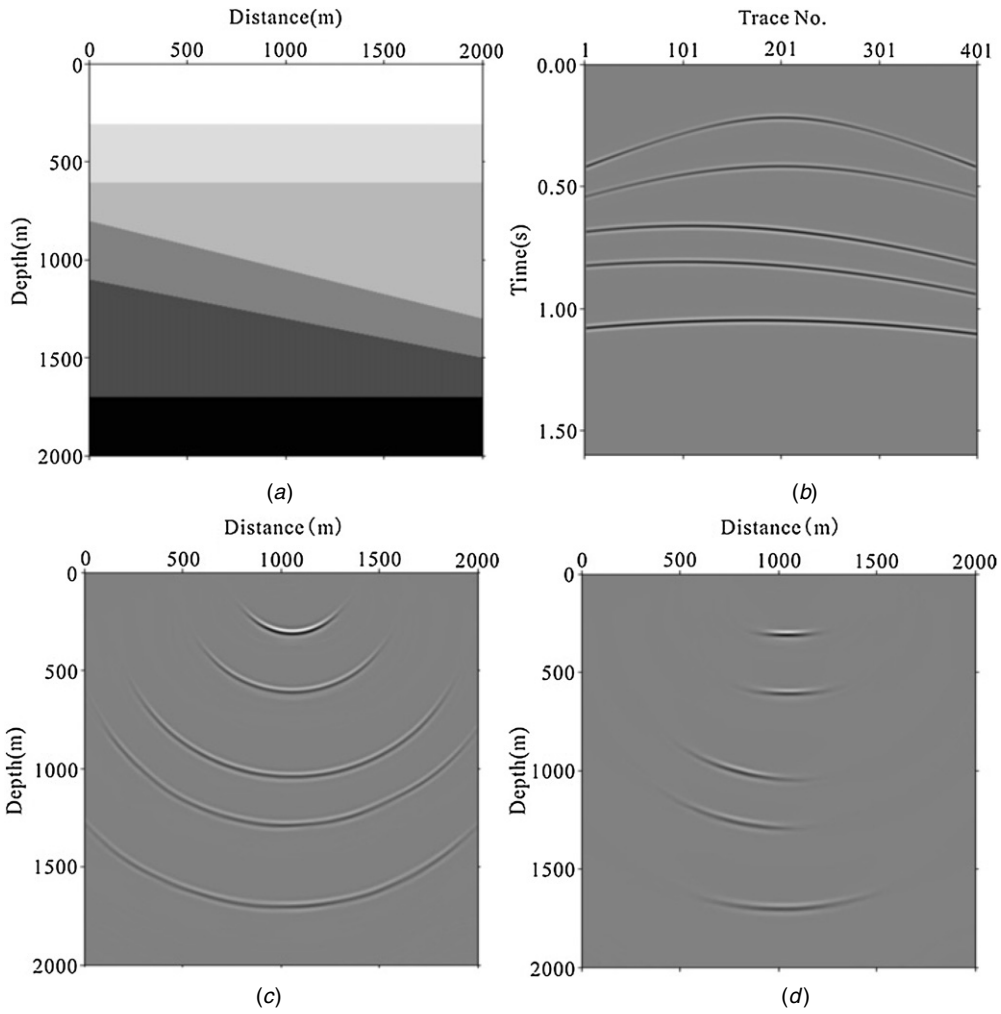

Figure 4. Local slant stack numerical analysis. (*a*) Velocity model, (*b*) single shot record, (*c*) Gaussian beam prestack depth migration of a single near-offset trace, and (*d*) Gaussian beam prestack depth migration of a beam centre after local slant stack.

by the two beams from the source and beam center. Similarly, $\overline{A}^{\mathrm{PS}}\left(\mathbf{x}, \mathbf{p}_s^P, \mathbf{p}_r^S\right)$ and $\overline{T}^{\mathrm{PS}}\left(\mathbf{x}, \mathbf{p}_s^P, \mathbf{p}_r^S\right)$ are the complex amplitude and complex travel time of PS-wave, and

$$\overline{T}^{\mathrm{PP}}\left(\mathbf{x}, \mathbf{p}_s^P, \mathbf{p}_r^P\right) = T_{\mathbf{x}_s}^P\left(\mathbf{x}, \mathbf{p}_s^P\right) + T_{\mathbf{L}_r}^P\left(\mathbf{x}, \mathbf{p}_r^P\right) \tag{12}$$

$$\overline{T}^{\mathrm{PS}}\left(\mathbf{x}, \mathbf{p}_s^P, \mathbf{p}_r^S\right) = T_{\mathbf{x}_s}^P\left(\mathbf{x}, \mathbf{p}_s^P\right) + T_{\mathbf{L}_r}^S\left(\mathbf{x}, \mathbf{p}_r^S\right). \tag{13}$$

Beams coming from both the source and beam center use the P-wave velocity to compute complex travel times $T_{\mathbf{x}_s}^P\left(\mathbf{x}, \mathbf{p}_s^P\right)$ and $T_{\mathbf{L}_r}^P\left(\mathbf{x}, \mathbf{p}_r^P\right)$ for the PP-wave image, while complex travel times $T_{\mathbf{x}_s}^P\left(\mathbf{x}, \mathbf{p}_s^P\right)$ and $T_{\mathbf{L}_r}^S\left(\mathbf{x}, \mathbf{p}_r^S\right)$ are computed with P- and S-wave velocities, respectively, for PS-wave image. Compared with the PP-wave, it has polarity reversal problem on the PS-wave seismic record, and direct migration for the PS-wave will seriously affect the migration result. Therefore, based on the polarity characteristics of the PS-wave records, the polarity has been corrected in the process of Gaussian beam prestack depth migration.

2.4. Local slant stack numerical analysis

The local slant stack is the key algorithm of the Gaussian beam migration method. It not only reduces traces involved in migration calculation and improves the computational efficiency significantly, but also gives the Gaussian beam migration method good directionality, which can make the subsurface structure have better imaging through decomposing a certain range of seismic records near a beam center into different outgoing directional local plane waves for wavefield extrapolation.

A six-layer model is given, as shown in figure 4(*a*), to present the local slant stack of the Gaussian beam migration method. The model contains some horizontal interfaces and dipping interfaces with different dip angles. A single-shot seismic record is generated using the ray tracing forward modeling method (figure 4(*b*)), and the shot is located at the center on the model surface. Figure 4(*c*) shows the Gaussian beam migrated image of a single near-offset trace without the local slant stack, where the energy is swung equally in all directions, which is similar to the Kirchhoff migrated image of a single trace. The local slant stack is performed on the seismic record nearby the near-offset beam center, and then data from this beam center are migrated with Gaussian beam migration method, as shown in figure 4(*d*). It can be seen that

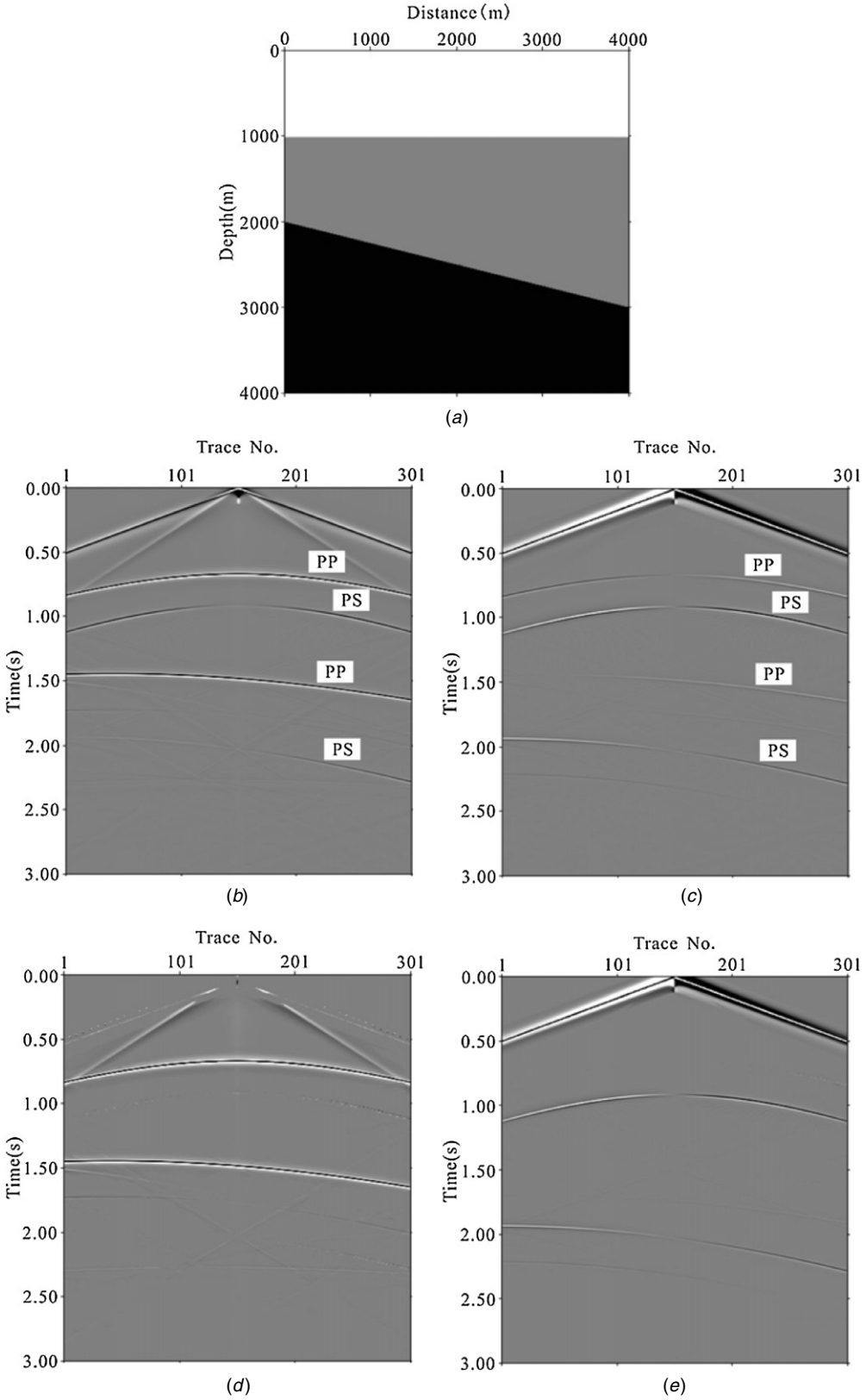

Figure 5. Migration test on dip layer model. (*a*) Velocity model, (*b*) *Z*-component single shot record, (*c*) *X*-component single shot record, (*d*) pure PP-wave seismic record by wavefield separation, (*e*) pure PS-wave seismic record by wavefield separation, (*f*) PP-wave image of *Z*-component shot record, (*g*) PS-wave image of *X*-component shot record, (*h*) separated pure PP-wave image and (*i*) separated pure PS-wave image.

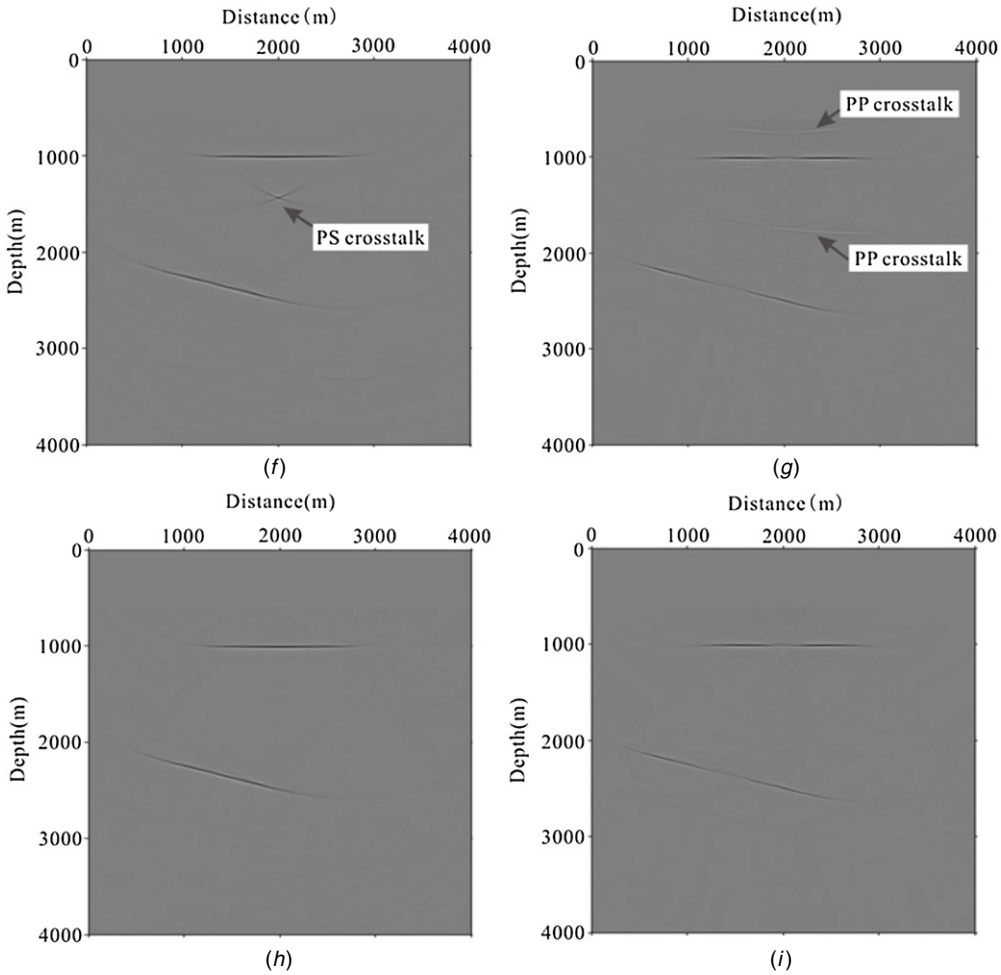

Figure 5. (Continued.)

the Gaussian beam migration has managed to discriminate among image directions through local slant stack. And whether flat or dipping reflectors, the image energy is only concentrated in the vicinity of the reflectors.

3. Numerical examples

3.1. Dip layer model

In this section, a simple dip layer model is used to test the multi-component Gaussian beam migration method (figure 5(*a*)). The P-wave velocities of model are $\alpha_1 = 3.0$ km s^{-1}, $\alpha_2 = 3.5$ km s^{-1}, $\alpha_3 = 4.0$ km s^{-1}, and the S-wave velocities are $\beta_1 = 1.7$ km s^{-1}, $\beta_2 = 2.0$ km s^{-1}, $\beta_3 = 2.3$ km s^{-1}, respectively. A single shot is located at the center on the surface. There are 301 receivers located on the surface with offsets from 1500 to 1500 m. Synthetic seismograms are generated using an elastic finite-difference algorithm. Figures 5(*b*) and (*c*) show the *Z*- and *X*-component records of the original seismic data, where the two components contain both PP- and PS-waves and polarity reversal can clearly be seen on the *X*-component. Figures 5(*d*) and (*e*) are pure PP- and PS-wave seismic records after wavefield separation in the affine coordinate system. The *Z*- and *X*-component seismic data are directly used to migrate and the results are shown in figures 5(*f*) and (*g*), respectively, where the PS-wave crosstalk on the *Z*-component and the PP-wave interference on the *X*-component are obvious (shown by arrow). Figures 5(*h*) and (*i*) show Gaussian beam migration images for the separated pure PP- and PS-waves, respectively. It is very clear from figures 5(*h*) and (*i*) that accurate PP- and PS-wave images of the subsurface reflectors are obtained without wavefield crosstalk. In the process of migration, the polarization of PS-wave has been corrected and the direct wave has been eliminated.

3.2. Relief model

To demonstrate the effectiveness of the new multi-component migration algorithm for nonhorizontal reflectors, a relief model is used. The model contains three interfaces, and the middle reflector is curved, as shown in figure 6(*a*). Synthetic seismograms are generated by the elastic finite-difference method and the source wavelet is the Ricker wavelet with a peak frequency of 25 Hz. There are 73 shots on the surface with 201 receivers per shot. The shot spacing is

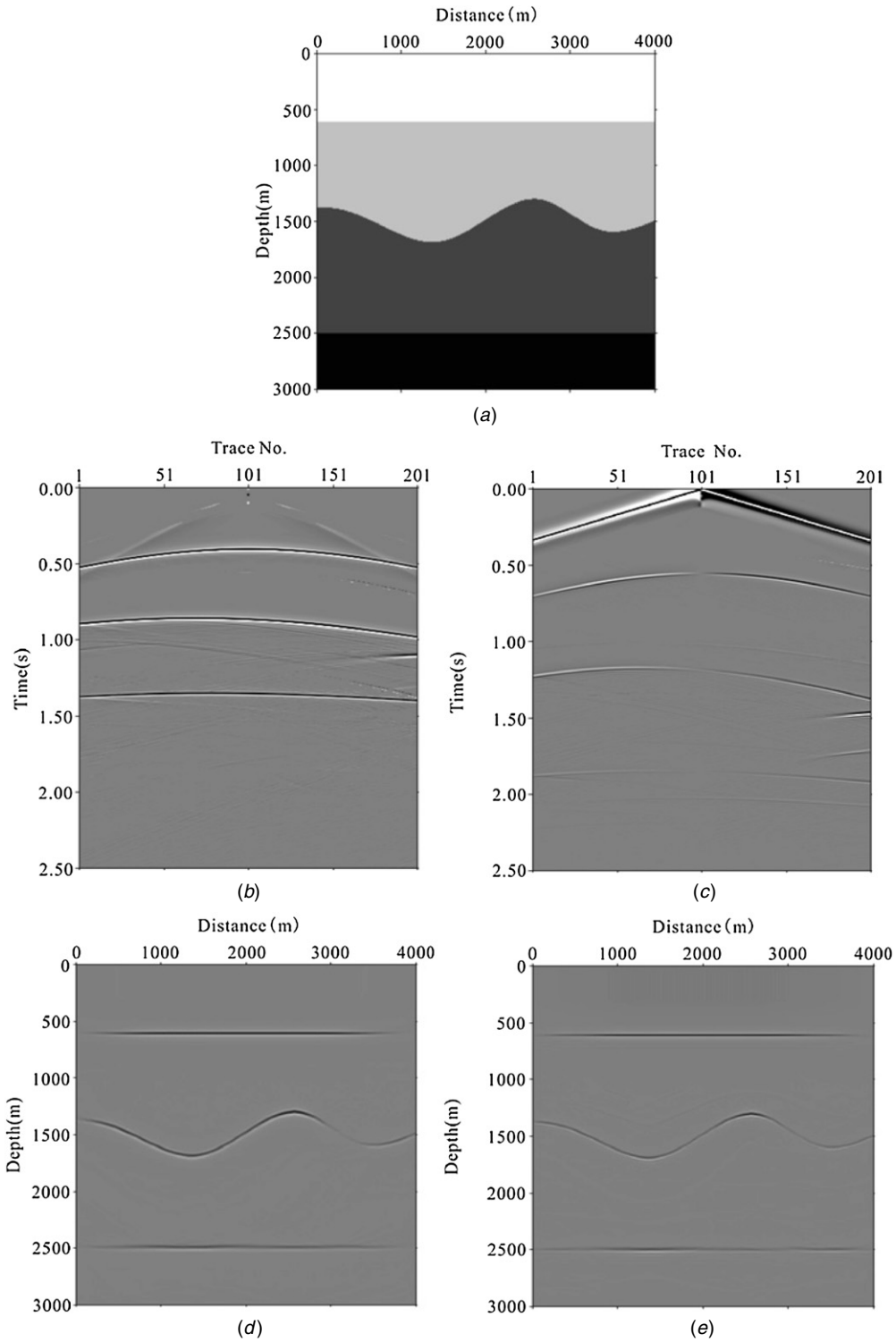

Figure 6. Gaussian beam migration test on relief model. (*a*) Velocity model, (*b*) pure PP-wave single shot record, (*c*) pure PS-wave single shot record, (*d*) PP-wave image and (*e*) PS-wave image. The velocities are $\alpha_1 = 3.0$ km s^{-1}, $\beta_1 = 1.7$ km s^{-1}, $\alpha_2 = 3.5$ km s^{-1}, $\beta_2 = 2.0$ km s^{-1}, $\alpha_3 = 4.5$ km s^{-1}, $\beta_3 = 2.6$ km s^{-1}, and $\alpha_4 = 5.0$ km s^{-1}, $\beta_4 = 2.9$ km s^{-1}, respectively.

40 m and the receiver spacing is 10 m. The travel time is 2.5 s with 1 ms sampling. The PP- and PS-waves are first separated from multi-component seismic data with the affine coordinate system transform. Figures 6(*b*) and (*c*) are the first shot seismic records of pure PP- and PS-waves and the PS-wave has polarity reversal. The stacked PP- and PS-wave Gaussian beam migration images are shown in figures 6(*d*) and (*e*), respectively. The polarization has been corrected for PS-wave image and the direct waves have been muted out. Comparing figures 6(*d*) and (*e*) with the original velocity

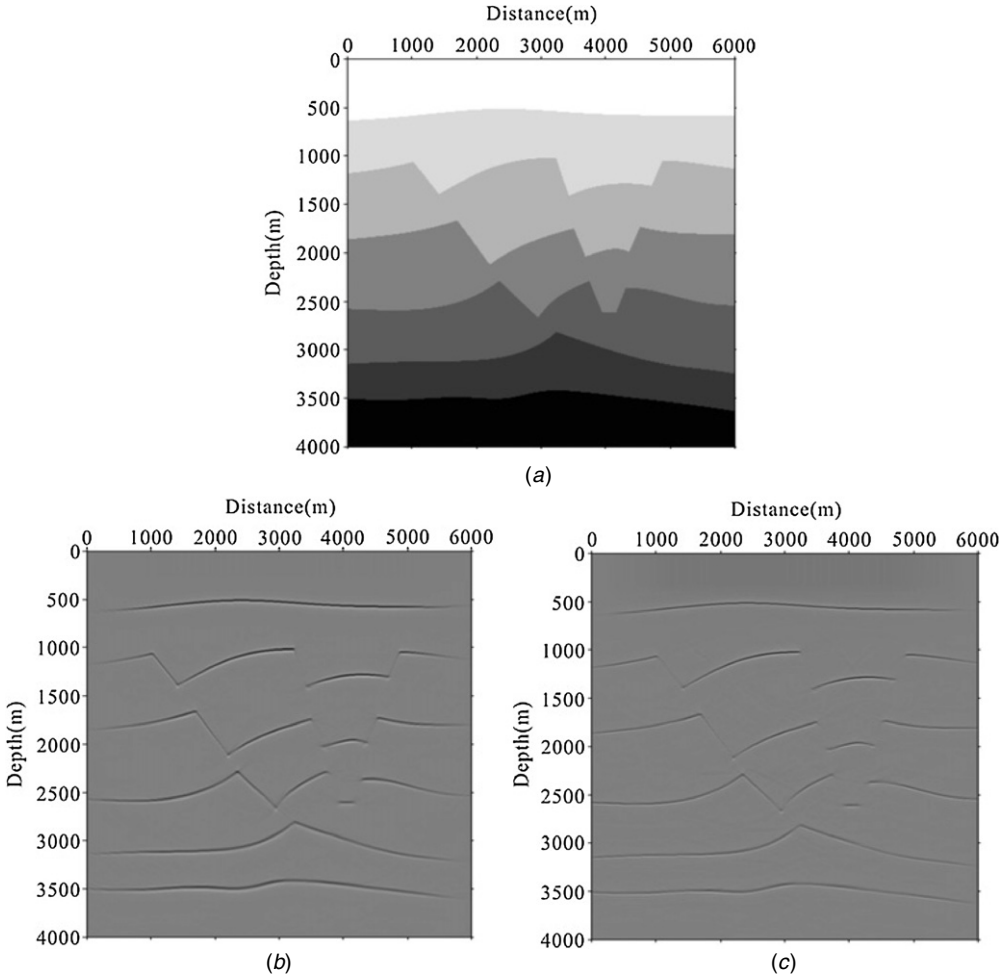

Figure 7. Gaussian beam migration test on fault model. (*a*) Velocity model, (*b*) PP-wave image and (*c*) PS-wave image. The velocities are $\alpha_1 = 3.0$ km s^{-1}, $\beta_1 = 1.7$ km s^{-1}, $\alpha_2 = 3.3$ km s^{-1}, $\beta_2 = 1.9$ km s^{-1}, $\alpha_3 = 3.6$ km s^{-1}, $\beta_3 = 2.1$ km s^{-1}, $\alpha_4 = 4.0$ km s^{-1}, $\beta_4 = 2.3$ km s^{-1}, $\alpha_5 = 4.3$ km s^{-1}, $\beta_5 = 2.5$ km s^{-1}, $\alpha_6 = 4.6$ km s^{-1}, $\beta_6 = 2.65$ km s^{-1}, and $\alpha_7 = 5.0$ km s^{-1}, $\beta_7 = 2.9$ km s^{-1}, respectively.

model (figure 6(*a*)), both PP- and PS-waves are accurately imaged at the reflector without wavefield crosstalk.

3.3. Fault model

The multi-component Gaussian beam migration method is further tested using a complex fault model, which contains seven layers, including complex fault and sag structures, as shown in figure 7(*a*). The elastic finite-difference method is used to generate the synthetic seismograms. There are 116 shots on the surface and the shot spacing is 40 m. Each shot has 341 receivers with offsets from 1700 to 1700 m. The sampling time is 3.2 s and the sampling interval is 2 ms. The PP- and PS-wave Gaussian beam migration images are shown in figures 7(*b*) and (*c*), respectively. It can be seen that the PP- and PS-wave layers match well in the migration profile. The fault and sag structures are well imaged, and the breakpoints are clear, which verifies the accuracy of the method for complex geological structures.

4. Field data example

To demonstrate the applicability of the method, we applied it to a multiwave seismic dataset acquired in the Songliao Basin in North Eastern China. The data total is 15 809 traces and the trace spacing is 25 m. The minimum offset for each shot is 400 m, and the maximum is 2375 m. The sampling time is 5 s and the sampling interval is 1 ms. The data are sampled to identify an igneous reservoir where a conventional P-wave image is not adequate to describe it. Figures 8(*a*) and (*b*) show three shot records of separated PP- and PS-wave seismic data. The PP- and PS-wave Gaussian beam migration images are shown in figures 8(*c*) and (*d*), respectively. It can be seen that PP- and PS-wave layers match well in the migration profile. For a subsurface hydrocarbon reservoir (between T4 and T5), the PS-wave migration obtains a clearer image than a PP-wave. A better image of subsurface reservoir structure may be acquired by combining PP- and PS-wave migration results.

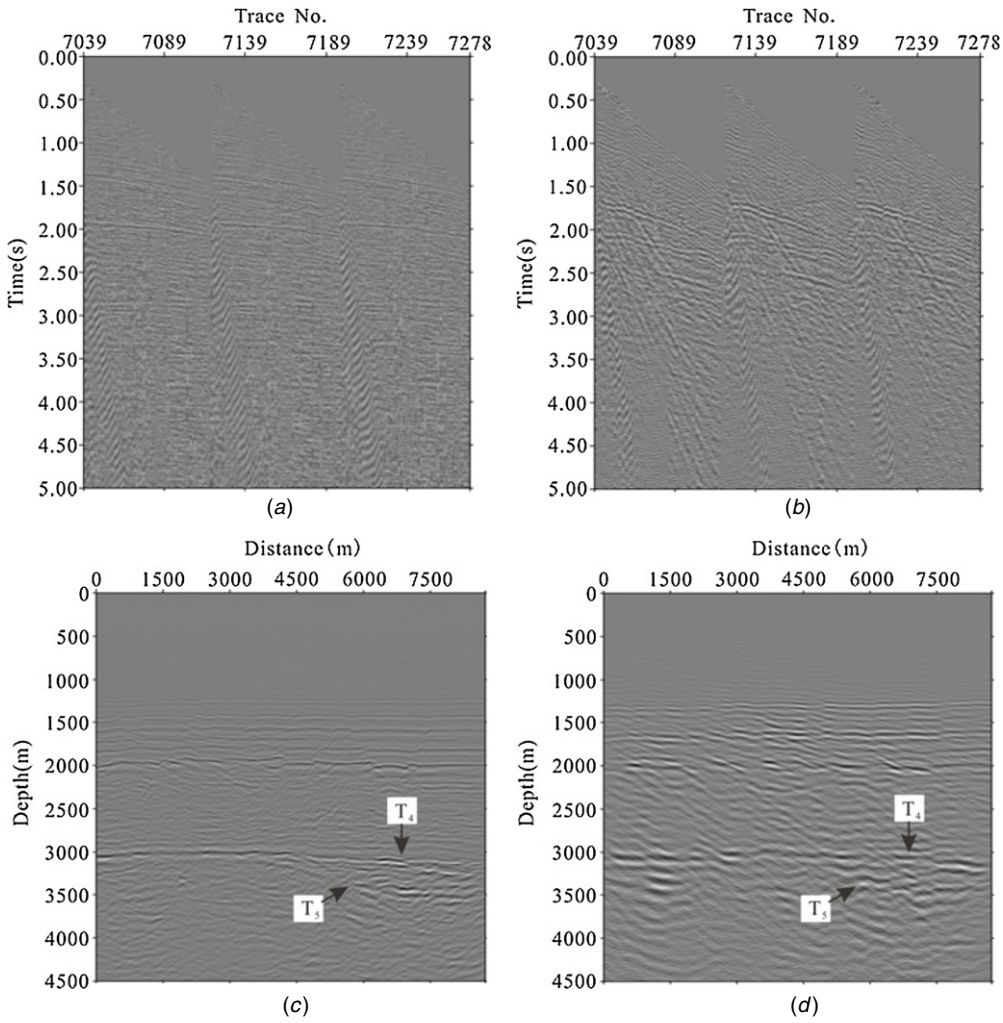

Figure 8. Gaussian beam migration test on field data. (*a*) Separated PP-wave seismic record, (*b*) separated PS-wave seismic record, (*c*) PP-wave image and (*d*) PS-wave image. In this figure, T4 represents reflections from the top of the igneous reservoir and T5 represents reflections from the bottom.

5. Conclusions

The multi-component Gaussian beam prestack depth migration method is an accurate and efficient migration method for multi-component seismic data. As numerical analysis has shown, the Gaussian beam migration method has outstanding advantages and an accuracy that rivals that of wave-equation migration and its efficiency and flexibility rival those of Kirchhoff migration through decomposing seismic records into different outgoing directional local plane waves with a local slant stack. Pure PP- and PS-waves are first separated from multi-component seismic data using the wave vector rotation transformation method in the affine coordinate system before wavefield extrapolation imaging. The accurate migration images of PP- and PS-waves in the numerical examples demonstrate the feasibility of the method. The field data test indicates that the method can be applied effectively to multi-component field seismic data, obtaining accurate images. Based on the complementarity of the multi-component seismic data for subsurface structural imaging, more accurate image can be obtained by making full use of PP- and PS-wave data.

Acknowledgments

This research was supported by the National Special Fund of China (nos 2011ZX05035-001-006HZ, 2011ZX05008-006-22, 2011ZX05049-01-02 and 2011ZX05019-003), the National Natural Science Foundation of China (no. 41104084), and the PetroChina Innovation Foundation (no. 2011D-5006-0303).

References

Červeny V 1983 Synthetic body wave seismograms for laterally varying layered structures by the Gaussian beam method *Geophys. J. R. Astron. Soc.* **73** 389–426

Červeny V 1985 Gaussian beam synthetic seismograms *J. Geophys.* **58** 44–72

Červeny V 2007 A note on dynamic ray tracing in ray-centered coordinates in anisotropic inhomogeneous media *Stud. Geophys. Geod.* **51** 411–22

Červeny V, Klimes L and Psencik I 2007 Seismic ray method: some recent developments *Adv. Geophys.* **48** 1–128

Červeny V, Popov M M and Psencik I 1982 Computation of wave fields in inhomogeneous media-Gaussian beam approach *Geophys. J. R. Astron. Soc.* **70** 109–28

Chang W F and McMechan G A 1987 Elastic reverse-time migration *Geophysics* **52** 1367–75
Chang W F and McMechan G A 1994 3D elastic prestack reverse-time depth migration *Geophysics* **59** 597–609
Dai T F and Kuo J T 1986 Real data results of Kirchhoff elastic wave migration *Geophysics* **51** 1006–11
Gray S H 2005 Gaussian beam migration of common-shot records *Geophysics* **70** S71–S77
Gray S H and Bleistein N 2009 True-amplitude Gaussian-beam migration *Geophysics* **74** S11–S23
Hale D 1992a Migration by the Kirchhoff, slant stack and Gaussian beam methods *Colorado School of Mines Center for Wave Phenomena Report* 121
Hale D 1992b Computational aspects of Gaussian beam migration *Colorado School of Mines Center for Wave Phenomena Report* 139
Hokstad K 2000 Multicomponent Kirchhoff migration *Geophysics* **65** 861–73
Hou A and Marfurt K J 2002 Multicomponent prestack depth migration by scalar wavefield extrapolation *Geophysics* **67** 1886–94
Hill N R 1990 Gaussian beam migration *Geophysics* **55** 1416–28
Hill N R 2001 Prestack Gaussian-beam depth migration *Geophysics* **66** 1240–50
Kuo J T and Dai T F 1984 Kirchhoff elastic wave migration for the case of noncoincident source and receiver *Geophysics* **49** 1223–38
Lu J, Wang Y and Yao C 2012 Separating P- and S-waves in an affine coordinate system *J. Geophys. Eng.* **9** 12–18
Nowack R L 2003 Calculation of synthetic seismograms with Gaussian beams *Pure Appl. Geophys.* **160** 487–507
Nowack R L, Dasgupta S, Schuster G T and Sheng J M 2006 Correlation migration using Gaussian beams of scattered teleseismic body waves *Bull. Seismol. Soc. Am.* **96** 1–10
Nowack R L, Wang P C, Kruse U and Dasgupta S 2007 Imaging offsets in the Moho: synthetic tests using Gaussian beams with teleseismic waves *Pure Appl. Geophys.* **164** 1921–36
Popov M M 1982 A new method of computation of wave fields using Gaussian beams *Wave Motion* **4** 85–97
Popov M M, Semtchenok N M, Popov P M and Verdel A R 2008 Reverse time migration with Gaussian beams and velocity analysis applications *70th EAGE Annu. Int. Meeting* (Extended Abstracts) p F048
Popov M M, Semtchenok N M, Popov P M and Verdel A R 2010 Depth migration by the Gaussian beam summation method *Geophysics* **75** S81–S93
Sun R and McMechan G A 2001 Scalar reverse-time depth migration of prestack elastic seismic data *Geophysics* **66** 1519–27
Wang Y and Nemeth T 1997 Multicomponent separation of PP and SS by a least-squares migration method: synthetic and field data tests *SEG 67th Ann. Int. Meeting* (Expanded Abstracts) pp 1222–5
Xie X B and Wu R S 2005 Multicomponent prestack depth migration using the elastic screen method *Geophysics* **70** S30–S37